Magnetic lipid nanovehicles synergize the controlled thermal release of chemotherapeutics with magnetic ablation while enabling non-invasive monitoring by MRI for melanoma theranostics

Lorena García-Hevia [a], Íñigo Casafont [b], Jessica Oliveira [a], Nuria Terán [b], Mónica L. Fanarraga [b], Juan Gallo [a,*], Manuel Bañobre-López [a,*]

[a] Advanced (Magnetic) Theranostic Nanostructures Lab. International Iberian Nanotechnology Laboratory, Avda. Mestre José Veiga s/n, 4715-330, Braga, Portugal
[b] Grupo de Nanomedicina. Universidad de Cantabria-IDIVAL, Herrera Oria s/n, 39011, Santander, Spain

ABSTRACT

Nowadays, a number of promising strategies are being developed that aim at combining diagnostic and therapeutic capabilities into clinically effective formulations. Thus, the combination of a modified release provided by an organic encapsulation and the intrinsic physico-chemical properties from an inorganic counterpart opens new perspectives in biomedical applications. Herein, a biocompatible magnetic lipid nanocomposite vehicle was developed through an efficient, green and simple method to simultaneously incorporate magnetic nanoparticles and an anticancer drug (doxorubicin) into a natural nano-matrix. The theranostic performance of the final magnetic formulation was validated in vitro and in vivo, in melanoma tumors. The systemic administration of the proposed magnetic hybrid nanocomposite carrier enhanced anti-tumoral activity through a synergistic combination of magnetic hyperthermia effects and antimitotic therapy, together with MRI reporting capability. The application of an alternating magnetic field was found to play a dual role, (i) acting as an extra layer of control (remote, on-demand) over the chemotherapy release and (ii) inducing a local thermal ablation of tumor cells. This combination of chemotherapy with thermotherapy establishes a synergistic platform for the treatment of solid malignant tumors under lower drug dosing schemes, which may realize the dual goal of reduced systemic toxicity and enhanced anti-tumoral efficacy.

1. Introduction

Traditional cancer therapies, mostly chemo- and radiotherapy, have represented a leap forward in cancer management aiding to revert the deadly trends of several cancer types bringing hope into this field. However, it is now clear that current treatment schemes are limited in one way or another. Drug resistance, adverse side effects, low therapeutic indices, poor bioavailability, lack of specificity, hypoxia, are some of the known limitations of these treatments [1–3]. Nanotechnology has been repeatedly proposed as a key player in the next anti-tumoral drug generation [4,5], particularly in the field of drug delivery, where some examples have already made an impact in the clinics (Doxil [6], Abraxane [7]). Although these nanoparticulated systems have shown enhanced therapeutic properties when compared to traditional drugs, they are based on the same principles and as such, they are also

limited. In the particular case of Doxil, liposomal vehicles present a series of disadvantages associated to the lack of affordable preparation methods, low drug loading capacity and solubility, poor stability, and rapid decomposition in the human body before the therapeutic effect can be achieved associated to premature drug release, as well as to oxidation and hydrolysis-like reactions of the constituting phospholipids [8,9]. A number of alternative therapeutic schemes have been recently proposed [10] [–] [12]. Unfortunately, these promising approaches are limited by their low response rate, justifying further studies aimed at developing combinatorial therapy strategies to generate effective synergies that can offer effective and long-lasting remission.

Magnetic hyperthermia (MH) has recently been successfully translated into clinical trials as an adjuvant treatment for glioblastoma multiforme and prostate cancer [13,14]. However, MH suffers from critical drawbacks mainly related to the need of high doses of MNPs at

the tumor site, which limits its definitive clinical implementation. In order to circumvent these limitations, new multimodal therapy approaches have been explored based on the synergistic integration of MH with other therapeutic modalities such as chemotherapy [15,16,25] [–] [17,30] [–] [24]. In particular, magnetic lipid-based hybrid nanosystems have been found to be efficient nanoplatforms to simultaneously incorporate magnetic nanoparticles and anti-cancer drugs for the combinatorial thermo-chemoterapeutic treatment of several types of cancer [16,19,21,24,27,31]. However, the vast majority of these reports are restricted to *in vitro* demonstrations. The lack of preclinical *in vivo* results is an indicator that most of the developed nanosystems fail when trying to confirm the thermochemo-therapeutic effect *in vivo*, pointing out the limited potential for the clinical translation of the growing research advances in this field. On the other hand, the scarce number of works involving *in vivo* validations make use of complex magnetic inorganic and polymeric structures which are surrounded by several synthetic and functional issues that also hamper their clinical translation, mainly related to the use of organic solvents and high synthesis temperatures, low yield of nanoparticles production, low MNPs/drug encapsulation efficiencies and aggressive treatment schemes (i.e. high number of administrations and hyperthermia doses) that would hardly find translation into the clinical practice [30,32–34]. In addition, intratumoral administration appears as the standard procedure *in vivo* to boost the efficacy of the proposed therapies [30]. However, this methodology is not applicable in a real human disease scenario. In this work, we demonstrate for the first time a synergistic therapeutic effect coming from the combination of chemotherapy with MH through a drug delivery system administered systemically. Further analysis of the results shows that MH application is the responsible for the synergistic effect observed as on one hand it accounts for the enhanced local controlled release of the drug, while on the other hand it damages tumoral tissues directly via thermal ablation. In addition, the magnetic properties of the proposed drug delivery system enables its use as imaging agent providing relevant information about the therapeutic process.

Here, we propose an effective, green and simple method to fabricate magnetic lipid nanocomposite vehicles (mLNVs) with enhanced antitumoral activity and low toxicity. The proposed nanostructure is based on a hydrophobic matrix composed of *Carnauba* wax. This natural compound is available commercially in a range of grades, being the T1 quality the one currently in use in the food [35] and pharma [36] industry. As such, it is approved by the FDA for its application in humans, in particular for end use under regulations 21CFR 184.1978 and 175.320, and GRAS -generally recognized as safe- and CTFA -Cosmetic, Toiletry, and Fragrance Association-listed. It possesses the highest melting point (~85 °C) among commercial natural waxes which makes it an attractive candidate for drug delivery applications as it minimizes pre-leakage of encapsulated drugs [37] [–] [39] and provides a highly stable platform for the formulation of nanovehicles. We have used this lipid matrix to co-encapsulate with high efficiency magnetic nanoparticles (MNPs), as imaging reporters in magnetic resonance imaging (MRI) and effectors in magnetic hyperthermia (MH) – also approved by the FDA and EMA for human application in these clinical areas –, and the chemotherapeutic drug doxorubicin (DOX), a potent anticancer agent used for many haematological and solid tumor malignancies [40]. Compared to liposomal nanocarriers, these lipid nanovectors show high stability, low cost, high encapsulation efficiency and enable a close control over the release process and profile through the combination of passive diffusion plus magnetic hyperthermia induction, thus "on demand" drug release, becoming a promising platform for particular DOX controlled delivery. Furthermore, this lipid phase also incorporates a lipophilic commercial fluorescent dye (DiO) as fluorescent reporter for *in vitro* studies/*ex vivo* biopsies. The whole structure is stabilized in water by the FDA-approved alkylphenolic surfactant Tween 80 (under regulation CFR172.840). All these components and their respective proportions were carefully chosen to combine diagnosis, drug delivery and therapy in a single platform.

Melanoma is the most aggressive and lethal form of skin cancer [41]. Metastatic melanoma accounts for nearly 80% of deaths, with a 5-year survival expectancy of ca. 14% [42]. Thus, to reduce mortality, early diagnosis is decisive for patient outcome [43]. Melanoma conventional treatments, that include surgery and chemotherapy, have proved mostly inefficient for patients with metastases. For instance, Murafenib and Dabrafenib treatments are short-lived and resistance to treatment eventually emerges [44] [–] [46]. Many other drugs used in melanoma treatment present adverse effects so they have been discarded [47]. One of the best ways to circumvent the high costs of introducing new active ingredients, is the development of biocompatible delivery systems to increase efficiency [48]. Drug delivery systems represent an effective strategy to deliver antineoplastic agents since they reconfigure the biodistribution of drugs providing: (i) enhanced circulation time with high stability, (ii) improved bioavailability, (iii) controlled drug release, (iv) decreased dosing, and (v) minimal toxic effects [49] [–] [51].

In this context, we introduce an integrated advanced theranostic nanoplatform, which combines four different tumor management concepts:

(i) provides longitudinal non-invasive imaging capabilities by MRI through the incorporation of biocompatible magnetic nanoparticles, for the diagnosis and follow-up of the tumor. (IMAGING)

(ii) enables the encapsulation and targeted delivery of chemotherapeutic drugs thanks to a hydrophobic core composed of a natural wax with excellent biocompatibility properties. (ENCAPSULATION)

(iii) permits a close control over the release process and profile through the combination of passive diffusion plus magnetic hyperthermia induction, thus "on demand" drug release. (CONTROLLED RELEASE)

(iv) provides a synergistic combination of chemo (DOX) and thermal (magnetic hyperthermia) therapies to enhance antitumoral efficiency and minimizes potential side effects through a reduction of the required dose (SYNERGISTIC COMBINATORIAL TREATMENT).

2. Materials and methods

Synthesis of mLNVs. A modified melt emulsification method was used for the preparation of mLNVs [52]. In a normal preparation, 200 mg of *Carnauba* wax (Carnauba wax T1 pharmaceutical grade was a generous gift from Koster Keunen Holland BV - Raambrug 3, 5531 AG Bladel, The Netherlands - intrinsic composition not disclosed) were mixed in a glass vial with a chloroform solution of Fe_3O_4 nanoparticles (prepared following a standard co-precipitation protocol) [53] containing 40 mg of Fe. To this solution, 250 μL of a chloroform solution of DiO (1 mg/mL) were added followed by a chloroform solution of DOX (40 mg DOX, 1 mL). This mixture was heated under a heat gun until all the chloroform had evaporated and the wax melted. At this point, 4.5 mL of milliQ water followed by 0.5 mL of a water solution of Tween80 (50 mg/mL) were added to the vial and the sample was ultrasonicated for 2 min at 25% power at 20 s working intervals. Immediately after the sonication, the vial was immersed in ice to solidify the lipid nanoparticles. Once cold, the formulation was centrifuged (3000 rpm, 10 min), the pellet discarded, and the supernatant freeze dried in the presence of sucrose (0.9% w/w) as cryo-protectant.

Characterization of mLNVs. Hydrodynamic diameters and ζ-potential values of the mLNVs formulations were determined using the dynamic light scattering (DLS) measurements (Horiba Scientific SZ-100 instrument). Transmission electron microscopy images (TEM) were obtained on a JEOL JEM-2100 microscope at an accelerating voltage of 200 kV. The amount of DOX loaded within the mLNVs formulations and DOX release profiles from the mLNVs formulations were determined by high performance liquid chromatography (HPLC) using anisocratic

gradient of water:acetonitrile (from 100% to 25:75%) and an Aeris 1.7 μm peptide XB-C18 column. UV (214 nm) and fluorescent detection (460 nm excitation, 560 nm emission) were used for the identification of DOX peak. Differential scanning calorimetry (DSC) was used for the determination of the melting point of the (m)LNVs by using a TGA/DSC1 STAR^e System from Mettler Toledo. mLNVs properties as magnetic hyperthermia effectors were investigated using a nB nanoScale Biomagnetics DM-100 instrument. *In vitro* and *in vivo* MH tests were performed in a Magnetherm instrument from Nanotherics.

2.1. Magnetic resonance imaging (MRI)

mLNVs and *in vitro*: MR imaging was performed in a 3T horizontal bore MR Solutions Benchtop MRI system equipped with 48 G/cm actively shielded gradients. To image the samples, a 56-mm diameter quadrature birdcage coil was used in transmit/receive mode. For the phantom imaging, samples at different concentrations (0–30 μM Fe) were prepared in milliQ water (300 μL) and pipetted into a custom printed PLA well plate. The phantoms of B16F10 cells were prepared by incubating 10^6 cells with PBS solutions of the mLNVs (at 3 different concentrations: 1, 10 and 100 mM) for 24 h. After the incubation and washing to remove free mLNVs, the cells were trypsinised and centrifuged to forms pellets. These pellets were then resuspended in agar (1%) to get a homogeneous gel and were pipette into 300 μL PCR eppendorf tubes to get the phantoms. All MR images of the phantoms were acquired with an image matrix 256 × 252, FOV 60 × 60 mm, 3 slices with a slice thickness of 1 mm and 0.5 mm slice gap. For T_2-weighted imaging, fast spin echo (FSE) sequences with the following parameters were used: T_E = 68 ms, T_R = 4800 ms, N_A = 15, A_T = 37 m 12s. The acquisition of T_2 maps was performed using multi-echo-multi-slice (MEMS) sequences with the following parameters: T_E = 10 values (0.015, 0.03, 0.045, 0.06, 0.075, 0.09, 0.105, 0.12, 0.135, 0.15s), T_R = 1400 ms, N_A = 5 and A_T = 32 m 00s. T_2 maps were reconstructed using ImageJ software (http://imagej.nih.gov/ij) following the standard equation: $S_n = S_0$ (1-e$^{-TEn/T2}$).

Mice imaging: To investigate the diagnostic/monitoring potential of the mLNVs, at the end of the treatment (day 14) the animals were perfused intravenously with formalin. Fixed whole mice were then imaged in 50 mL Falcon tubes in a 3T horizontal bore MR Solutions Benchtop MRI system. FSE (fast spin echo) T_2-weighted sequences were used to locate the tumor region. Then, MEMS sequences were used to acquire T_2 maps with the following parameters: T_E = 15 values (15, 30, 45, 60, 75, 90, 105, 120, 135, 150, 165, 180, 195, 210 and 225 ms), T_R = 1450 ms, N_A = 10 and A_T = 46 m 24s. T_2 maps were reconstructed using ImageJ software (http://imagej.nih.gov/ij) following the standard equation: $S_n = S_0$ (1-e$^{-TEn/T2}$). Tumor ROIs were drawn manually over 3–6 ca. axial slices.

Cell Culture. B16F10 murine malignant melanoma cells (ATCC CRL-6475) were grown in Dulbecco's Modified Eagle's Medium (DMEM) supplemented with 10% foetal bovine serum and 1% antibiotic and was incubated under 37 °C within 5% CO_2 atmosphere.

Cellular drug internalization. B16F10 cultures were treated with free DOX as a positive control, and mLNVs-DOX (2 μg/mL dose) for 2, 4 and 6 h. Cells were fixed with 4% paraformaldehyde and stained with Hoechst. Confocal images were taken with a Carl Zeiss inverted microscope attached to the LSM 780 confocal system and the fluorescence intensity was measured by ImageJ software (software: ZEN 2010). Images are pseudocoloured.

***In vitro* magnetic hyperthermia treatment.** 4×10^5 B16F10 cells were cultured in a 35 mm^2 plate for 24 h and then exposed for 4 h mLNVs formulations. Then, plate were placed in live cell alternating magnetic field exposure system which has an ergonomic design and enables physiological temperature control and a 5% CO_2 atmosphere (NanoTherics). Cells were exposed to 224 kHz, 13 A, 27.6 W for 1 h. At 48 h after hyperthermia, cells were washed twice with Hank's balanced salt solution and the cell viability studies were performed.

Cell viability assays and cell cycle analysis. To evaluate cell death, two methods were used: Live/Dead viability/cytotoxicity kit (Molecular Probes) and the Trypan blue exclusion assay. For live/death kit samples were incubated for 20 min at 37 °C and viewed under a fluorescence microscope, dead cells (stained red) and live cells (stained green). B16F10 cultures were stained with Trypan Blue (10%) and live and dead cells were counted with a Neubauer's chamber under a light microscope. Cell cycle was measured by flow cytometry of a suspension of fixed cells stained with Hoechst dyes (Bisbenzimide) using a Cyto-FLEX equipment (Bectam Coulter), data were analyzed using the CytExpert Software.

Confocal Microscopy Imaging. Cells were fixed in 4% paraformaldehyde. Cortical actin was stained with phalloidin-tetramethylrhodamine B isothiocyanate (Sigma-Aldrich) and DNA (nucleus and chromosomes) with Hoechst dye (Sigma-Aldrich). Microtubules were immunolabelled with the monoclonal anti-tubulin antibody (B512) coupled to an Alexa Fluor 488 conjugated secondary goat anti-mouse immunoglobulin G (IgG).

TEM Cell Images. Transmission electron microscopy on melanoma cultures was performed on 70 nm Araldite sections of cell pellets fixed with 3% glutaraldehyde in 0.12 M phosphate buffer and postfixed in 1% buffered osmium tetroxide, dehydrated in a graded acetone series, embedded in Araldite, sectioned and stained with uranyl acetate. These samples were observed using a JEOL JEM 1011 microscope.

Animal studies. Experiments were designed and performed to minimize the use of animals. C57BL/6 mice (8–10 weeks old) have been housed with a 12-h light/dark cycle with free provision of food and water at the Experimentation Service (SEEA) of the University of Cantabria (CEA ES390750000849). Animal experimentation was approved by local authority "Consejería de Medio Rural, Pesca y alimentación" project number: PI-09-16. Animals were maintained, handled and slaughtered in accordance with the directives.

Tumor induction. Tumoriogenesis was induced according to protocol established by García-Hevia et al. [54]. A melanoma cell suspension (5×10^5 cells in 100 μL DMEM) was subcutaneously injected in the interscapular region of mice.

Evaluation of anti-tumor and hyperthermia effects in a mouse melanoma tumor model. When the tumor masses were palpable (ca. 7 days) the mice were randomly divided into 5 groups (n = 8). The groups were designated as: saline control (group 1), free DOX (group 2), mLNVs-MH (group 3), mLNVs-DOX (group 4) and mLNVs-DOX-MH (group 5). Mice in groups 2, 4 and 5 were treated by intravenous injection once every other day for three days at a concentration of 2.5 mg kg^{-1} DOX, groups 1 and 3 were treated with the same volume of saline serum and mLNVs respectively. After the administration, mice in groups 3 and 5 were anesthetized by inhalation (1% isoflurane), placed in a water-cooled induction coil (50 mm internal diameter, nine turns) with the tumors located in the centre of the coil, and exposed to 174.5 kHz, 23 mT for 1 h. The body weight and tumor size of each animal were monitored daily. The estimated tumor volume was calculated using the following formula: Tumor volume (mm^3) = d^2 x D/2 where d and D are the shortest and longest diameter in mm, respectively. At the end of the experimental period, the mice were euthanized and their tissues dissected and harvested.

***In vivo* bio-distribution.** The amount of Fe in the major organs of the mice was quantified via inductively coupled plasma optical emission spectrometry (ICP-OES). Harvested organs (tumor, brain, heart, lung, kidney, spleen, liver, intestine and muscle) were immersed in formalin. Each organ was weighted (wet) and then calcined (450 °C, 12h) individually in glass vials to remove organic matter. Leftover ashes were dispersed in concentrated HCl (37%) overnight, diluted to 10 mL with milli-Q water and analyzed via ICP-OES.

Frozen tissues. Tissues were frozen in OCT compound (Sakura, Tokyo, Japan) and sectioned at a thickness of 6 μm with cryostat. The sections were fixed in paraformaldehyde 4% and stained with Hoechst.

Histopathological examination. Excised tissues were fixed in 10%

formalin, embedded in paraffin, sectioned (4 μm thick), deparaffinised, and stained with Hematoxylin-Eosin.

Prussian blue assay. Samples were post-fixed in 10% formalin, buffered and dehydrated for later inclusion in paraffin. For its analysis, sections of 4 μm were made for subsequent staining with Hematoxylin-Eosin and Prussian blue for the detection of iron in the different sections under study.

Statistical analysis. ANOVA tests were used to compare groups. When ANOVA resulted significant, pairwise comparisons and Student's t-test were conducted. These statistical analyses were done using SPSS, version 19.0.

3. Results and discussion

mLNVs formulation. The procedure followed for the preparation of the mLNVs is based on a modified melt-emulsification method as illustrated in Figure S1. In this protocol, a hydrophobic solution is mixed with an aqueous phase and ultrasonicated to obtain a stable formulation. As mentioned in the introduction, the matrix of the hydrophobic phase is composed of *Carnauba* wax, and it incorporates at the same time magnetic nanoparticles (MNPs), the chemotherapeutic drug DOX and a lipophilic commercial fluorescent dye (DiO). The aqueous phase presents a simpler composition been formed only by milli-Q water and the alkylphenolic surfactant Tween 80 (**Fig. 1**A). The main morphological, structural and magnetic characterization results of the iron oxide MNPs precursors are displayed in Figure S2, whereas the composition and physico-chemical properties of the final mLNVs formulation used throughout this work are summarized in Table 1. To define this formulation, its composition was optimized with respect to the magnetic and chemotherapeutic agent loading. In order to work as a theranostic agent, the concentrations of both reporter and effector agents have to be balanced to reach an active concentration at the same time. In this case, MNPs (MRI) and DiO (fluorescent optical imaging) act as reporting species, while MNPs and DOX participate both as therapeutic agents. The concentration of DiO was fixed from the beginning to a level at

Table 1
Summary of the composition and physico-chemical properties of mLNVs.

Formulation*	Wax	Tween80	DiO	MNPs	DOX
mLNVs	200 mg	12.5%	0.125%	2.5%	20%
Physico-chemical properties					
D_h/PI	204 ± 4 nm/0.16 ± 0.1		$\lambda_{emission}$	506 nm (350 nm exc)	
$\zeta_{potential}$	-56 ± 2 mV		**EE**	>85% (DOX); >99% (MNPs)	
Organic content	76.4%		r_2	214 ± 20 mM-1 s-1 (1.41 T)	
M_s	4 emu/g		**SAR**	517 W g-1 (869 kHz, 25 mT, 1 mgFe/mL)	

(*) all values in the composition on of the formulation are w/w relative to the amount of wax.

which the particles were clearly observed by confocal microscopy (Fig. 2). The concentration of DOX was fixed to 20% after the quantification of encapsulated drug suggested that, at this concentration, the encapsulation efficiency already begins to drop (Supporting Table 1). At 20% DOX the encapsulation efficiency was still high with reproducible values above 85%. The magnetic loading of the mLNVs was set to a level comparable to the amount reported from commercial T_2 contrast agents (Endorem®, 15 μmol Fe/kg) for human application. In the case of the MNPs, the encapsulation efficiency was above 99% due to the high affinity of the oleic acid coating of the nanoparticles for the wax (Supporting Table 1). According to these design considerations, the reaction yield can be calculated with respect to the different components. Thus, in terms of the drug the yield of the reaction after purification was of >85%, whereas in terms of wax the yield was around 60%. In terms of MNPs the yield was much lower, around 8%, due the heavier nature of MNPs that accumulate them in the pellet during centrifugation.

mLNVs characterization. The selected formulation (mLNVs 30% MNPs 20% DOX, mLNVs-DOX from now on) was fully characterized from a physico-chemical point of view. Regarding the size of the nanocomposites, DLS analysis provided a hydrodynamic size of around 200
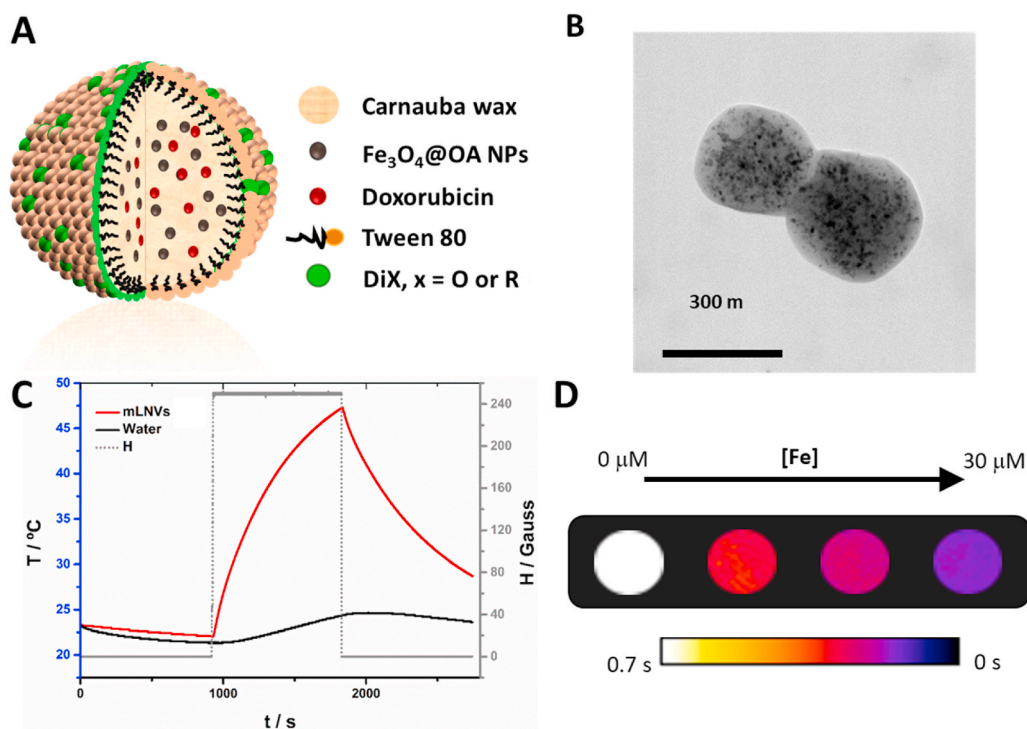

Fig. 1. (A) Schematic representation of the mLNVs. (B) TEM micrograph of mLNVs. (C) Heating profile of a mLNVs-DOX (red line) dispersion at a concentration of 1 mg_Fe/mL under an alternating magnetic field of 25 mT and 869 kHz. (D) T2 map of phantoms of serial dilutions (0–30 μM Fe) of mLNVs-DOX. (For interpretation of the references to colour in this figure legend, the reader is referred to the Web version of this article.)
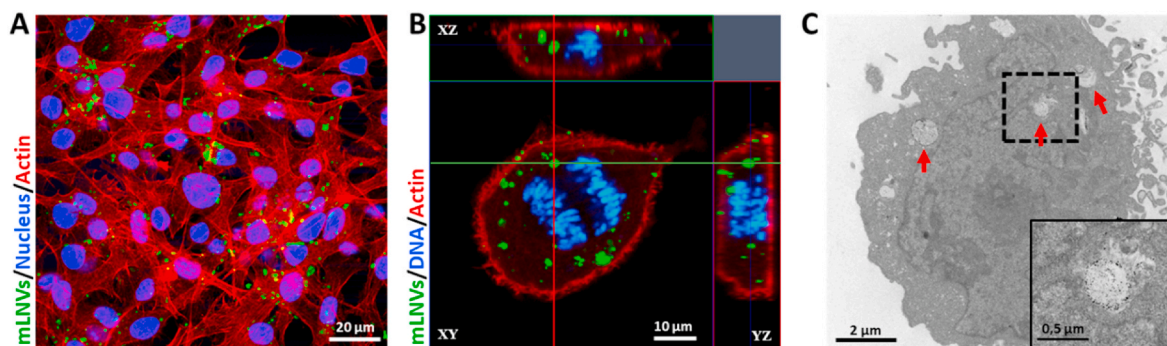
Fig. 2. Localization and distribution of mLNVs in malignant melanoma cells. (A) Confocal lateral projection images of B16F10 melanoma cells exposed to mLNVs (green) during 12 h. Actin (red channel) and nucleus (blue) were stained with TRITC-phalloidin and Hoechst respectively. (B) Confocal lateral projection images of internalized mLNVs (green) in a cell undergoing anaphased, where the blue color represents the chromosomes of the cell while the red is actin. (C) TEM image of a section of a melanoma cell exposed to mLNVs-DOX during 24 h (Inset) High magnification of the boxed area of the cytoplasm of the cell. Arrows point at intracellular mLNV particles. (For interpretation of the references to colour in this figure legend, the reader is referred to the Web version of this article.)

nm with a narrow polydispersity index (0.16). The stability of the formulations was assured by periodical DLS measurements where the formulations maintained their size within, at least, 6 months from the synthesis. This colloidal stability is probably a result of the electrostatic repulsion between particles due to the high negative ζpotential (−56 mV) of the mLNVs, which is attributed to the presence of fatty acids from the carnauba wax. Unlike most other lipid systems, the high melting point of *Carnauba* wax (82–86 °C) enabled direct TEM imaging. Analysis of TEM images acquired at 200 kV showed a spherical shape of the mLNVs with an average size of between 300-400 nm (Fig. 1B). TEM images clearly show the presence of darker smaller nanoparticles (MNPs) inside the mLNVs. The homogeneity of the characteristic spherical shape of the mLNVs was also confirmed by SEM (Figure S3A). Regarding the optical properties of the mLNVs, from their UV–Vis spectra, the extinction properties of the nanocomposites are consistent with subwavelength sized dielectric spheres (Figure S3B). The incorporation of DiO is not reflected in the shape of the spectra, probably due to the low concentration. However, the presence of DOX can be observed in mLNVs-DOX as a double shoulder in the region around 500 nm, matching the position of the visible peak from free DOX [55]. Thermogravimetric analysis of the samples confirms that the original magnetic loading of the formulations is preserved throughout the preparation and purification protocols, as a final loss of mass of 76.4% was recorded (Figure S3C). Even though the presence of DiO was not observed in the UV–Vis spectra, its presence in the formulation is distinguishable by fluorescence spectroscopy, were a strong peak at ca. $\lambda_{max} = 506$ nm is observed (Figure S4). In the final formulation containing DOX, this peak presents two shoulders at longer wavelengths (547 and 592 nm) coming from the released DOX. Encapsulation inside the mLNVs quenches DOX fluorescence but, the inherent red signal from DOX is recovered upon drug release. Material analysis via XRD shows two predominant peaks at low theta (20–25) coming from the wax. Smaller peaks from magnetite (COD 96-900-2318) can be observed upon magnification of the areas of interest, confirmation once again of their nature and presence in the mLNVs (Figure S5A). Regarding the magnetic properties, hysteresis loops (magnetization *vs.* applied magnetic field curves) were measured in a squid magnetometer between −20 and + 20 kOe at room temperature (Figure S5B). Results indicate that the magnetic nature of the MNPs is preserved after their incorporation into the lipid matrix. The final mLNVs showed a superparamagnetic behavior with negligible coercive forces and remanence. The hysteresis observed in the low field magnification area is mostly an artefact due to residual eddy currents trapped in the superconducting coil.

The functional properties of the mLNVs were then investigated. The diagnostic/monitoring capacity of the formulations rely on the well-described ability of MNPs to alter the relaxation time of water protons in their vicinity. The transversal relaxivity of mLNVs was measured at a

clinical field of 1,41T and, considering that commercial T_2 contrast agents present r_2 values of around 50 mM^{-1}s^{-1} at this same field (Resovist, 61 mM^{-1}s^{-1}; Endorem, 41 mM^{-1}s^{-1}) [56], the r_2 of mLNVs-DOX calculated to be 214 mM^{-1}s^{-1} is nearly 5 fold larger than that of commercial CAs. To translate these findings into imaging potential, phantoms at different Fe concentrations of the formulations were imaged by MRI at 3.0T. Images shown in Fig. 1D demonstrate the ability of the formulation to generate contrast. Transverse relaxivity values calculated from T_2 maps corroborate the good performance of the formulation with r_2 value of 249 ± 16 mM^{-1}s^{-1} at 3.0T (see experimental data and calculation details in Figure S5C in the SI). Regarding the ability of the formulation as MH effectors, its specific absorption rate (SAR) was studied under adiabatic conditions at a field of 25 mT and a frequency of 869 kHz. Results displayed in Fig. 1C show that mLNVs-DOX were able to increase the temperature of the solution efficiently over the course of a 15 min MH pulse. mLNVs-DOX presented a SAR value of 517 W g^{-1} (Table 1). In order to understand the effect of the alternating magnetic field frequency on the SAR of the mLNVs, a systematic calorimetric characterization study was performed in a wide range of frequencies under a fixed field intensity. The SAR values obtained are displayed in Figure S5D and show a linear relationship of SAR within the whole range of frequencies tested, as expected from the theoretical field frequency linear dependence of SAR. Even though a direct comparison of the hyperthermia performance of mLNVs with that of other reported systems is hindered by the big variability of physico-chemical characteristics among the magnetic objects (i.e. size, shape), as well as by the experimental parameters inherent to the hyperthermia measurements (i.e. frequency and intensity of the magnetic field), still some general considerations can be made. First, the heating ability of the magnetic lipid carriers is > 2-fold higher than that of free equivalent ~10 nm hydrophilic pseudo-spherical iron oxide nanoparticles measured at similar frequencies and magnetic fields [57,58], including FDA-approved magnetite nanoparticles such as Ferumoxytol (~250 W/g),[34] Resovist (106 W g^{-1}) [59] and Feridex (115 W g^{-1}) [60]. Second, the confinement and distribution of MNPs inside the wax matrix, opposite to previous reports that have also highlighted that three-dimensional nanoparticles arrangements can generate demagnetizing effects that result in a drastic reduction on the heating performance of iron oxides [61,62], induce a significant increase in the SAR. This is particularly relevant to minimize SAR losses *in vitro* as consequence of inhomogeneous particle aggregation and the annihilation of the Brownian contribution to the total heating performance [63]. Magnetic dipolar interactions due to the three-dimensional arrangements of MNPs when confined in the solid lipid matrices, together with inter-particle magnetic interactions between magnetic wax particles, could justify this observation, as it has been already demonstrated in other magnetic polymeric carriers [64]. The performance of mLNVs-DOX as responsive

drug delivery systems was then investigated. In most of the lipid systems reported to date, the release of encapsulated drugs is only passive, controlled by the concentration gradient stablished between particles and media, and the relative solubility of the drug in each. In this case we propose that the presence of MNPs in mLNVs can be profited to add an extra level of control over the release process and its specificity. The combination of passive drug release with MH will impact the release profile of the drug. To demonstrate this principle, first the release of DOX from the mLNVs-DOX was characterized under passive Fickean conditions. A two-container setup was used for this purpose and the amount of DOX released was monitored against time through HPLC measurements (Figure S6A and S6B). Then, the same setup was used to characterize the release profile under mild magnetic hyperthermia induction (174.5 kHz, 23 mT). MH was applied continuously during the first 2 h of release. The release of DOX is statistically faster under MH than under passive conditions, with over a 70% increase in released DOX. It is worth noticing here that at the concentration used for these tests, the T of the solution containing the formulation did not significantly increase further than the one under passive conditions (Figure S6C). In order to extract more information about the release mechanism displayed under passive and MH-induced conditions, previous release data were fitted to different mathematical models of drug release (Supporting Table 2). In the case of the passive release, the model that produces the best fitting was Korsmeyer-Peppas', with an n value of 0.56. An n value between 0.45 and 0.89 means that the release is controlled by a mixture of case I and case II transport, being a result of diffusion plus 'erosion' of the carrier. However, when the experiments are performed under MH conditions the model that better describes the release is Higuchi's, which means that the release is controlled fully by diffusion. These data, together with the fact that the incorporation of magnetic nanoparticles in the LNVs did not change the high melting point of the wax solid matrix (see DSC data in Figure S7A), confirm that the extra level of control over the release process is only mediated by the thermal effect induced by the magnetic nanoparticles under an alternating magnetic field, and allow us to hypothesize that the heat generated by the MNPs under MH conditions, increases the diffusion of DOX from the mLNVs, but it is not enough to fully melt the LNVs matrix (local melting will contribute to an enhanced diffusion). This hypothesis is further supported by TEM images of the formulations acquired after the MH treatment that show that the integrity of the mLNVs is preserved (Figure S7B).

Cell internalization and intracellular distribution. To investigate the ability of mLNVs to enter cells as well as their intracellular distribution, we examined melanoma cell cultures incubated with mLNVs during 24 h using confocal laser scanning microscopy (CLSM) and TEM. Fig. 2A shows a confocal image of melanoma cells with mLNVs (green) at 24 h post incubation. It can be observed that mLNVs were located in the intracellular space or the cytoplasm of the cells, consistent with intracellular translocation of vesicles from the plasma membrane along microtubules in the minus direction toward the centrosome/microtubule-organizing region of the cell [65]. CLSM lateral projection imaging at a single cell level served to confirm that mLNVs were intracellular (Fig. 2B). Additional CLSM images at lower cell density are also shown in Figure S8 further supporting this fact. It is important to highlight that the green fluorescence coming from the mLNVs does not correspond to a particle post-preparation staining, but to the green fluorescence of DiO decorating the mLNVs and incorporated during the fabrication procedure. Similar results were obtained with TEM (Fig. 2C) where mLNVs-DOX can be observed penetrating the membrane and distributed throughout the cell cytoplasm. To unequivocally identify these structures as mLNVs, EDX spectra were acquired to show the presence of Fe in the area as opposed to other areas of the cell (Figure S9). Furthermore, these pictures also illustrate the effects of mLNVs-DOX in cell morphology which induces typical features of necrosis: loss cell membrane integrity, collapse of organelles and lysis of the cell.

mLNVs are bio-compatible and mLNVs-DOX show anti-tumor effect

in melanoma cell line. We first examined whether mLNVs exhibit anti-tumor activity towards a melanoma cell line. The cytotoxicity of mLNVs and mLNVs-DOX compared to free DOX were evaluated after incubating melanoma cells with these samples at a series of concentrations from 0.5 to 5 μg/mL for 24 and 48 h (Fig. 3A and B). No evidence of alteration in cell morphology nor significant inhibition effects against melanoma cells was observed after exposure to mLNVs in the whole timeline of incubation (Figure S10). On the contrary, free DOX and mLNVs-DOX induce a dose-dependent response in malignant melanoma cells. Interestingly, DOX loaded mLNVs induced an important decrease in half maximal inhibitory concentration (IC_{50}) compared to the free drug: from 3.9 ± 0.9 to 1.7 ± 0.6 μg/mL at 24 h and from 1.5 ± 0.6 to 0.9 ± 0.2 μg/mL at 48 h (Table 2). In conclusion, mLNVs-DOX showed higher cytotoxicity activity than free DOX, presenting an evident difference in the cell culture at concentrations around 2 μg/mL (Figure S10). All these cell viability results were corroborated by flow cytometry experiments of DNA fragmentation to determine apoptosis (Figures S11, S12 and S13), showing that mLNVs-DOX work as effective anti-tumor agent at the cellular level.

mLNVs-DOX accelerate intracellular DOX accumulation *in vitro*. To elucidate why encapsulated DOX showed an enhanced effect over free DOX at the same drug concentration, a complete *in vitro* DOX release study was performed. Fig. 3C shows representative confocal microscopy images of B16F10 melanoma cells treated with free DOX compared to mLNVs-DOX following 2, 4 and 6 h of incubation. Images show that DOX accumulation in the nucleus (blue channel) from both free and encapsulated DOX was similar after 2 h. In contrast, a fast rise in fluorescence intensity was observed in cells treated with mLNVs-DOX at 4 and 6 h (see Figure S14A in the SI). Despite the co-localization of the drug in the nucleus being evident by eye, we validated these observations through a Pearson correlation analysis, which gave Pearson correlation coefficients >0.90 in all the cases. To further corroborate this effect, this study was repeated by flow cytometry where similar results were obtained (Figure S14B). This crucial result indicates that our mLNVs-DOX accelerate intracellular DOX accumulation that could be one of the main reasons to explain why mLNVs-DOX is more efficient compared to free DOX. This faster intracellular drug internalization mediated by wax vehicles could be of high interest to avoid drug resistance phenomena in tumor cells, which are mostly derived from the limited bioavailability of the drug at the tumor site and the corresponding sub-lethal drug concentration at cellular level. Further studies in this direction are underway.

mLNVs display an important potential as contrast agent by MRI *in vitro*. In order to validate our mLNVs as a new theranostic nanocomposites, the next study was designed to determine their potential as diagnostic agents by MRI. For this purpose, melanoma cell cultures were incubated with increasing concentrations (1, 10 and 100 mM) of mLNVs-DOX. The results show a concentration dependent contrast decrease (as expected from a T_2 contrast agent), consistent with a higher final concentration of mLNVs uptaken by the cells as the incubation concentration increases (Figure S15).

Synergistic effects with thermo/chemotherapy inhibit melanoma cell viability. To evaluate the effect of hyperthermia *per se* and combined with chemotherapy on malignant melanoma cells *in vitro*, we examined the cytotoxicity of mLNVs and mLNVs-DOX after exposure to an alternating magnetic field (AMF) at 20 mT and 224 kHz for 1 h. For this purpose, we used a live cell AMF exposure system with a design that enables temperature and atmosphere (5% CO_2) control (Figure S16) thus cells grow continually without additional stress factors (other than the AMF treatment). Two complementary methodologies were used, a Trypan blue exclusion test (Fig. 4A) and a commercial live/death kit based on calcein-AM and ethidium homodimer-I test (Fig. 4B). Both independent studies revealed similar results. For mLNVs-DOX alone, a moderate number of necrosed cells were observed (85% viability) when they were incubated at a low concentration (0.5 μg DOX/mL) suggesting a sub-optimal DOX dose. Interestingly, there is a remarkable increase in
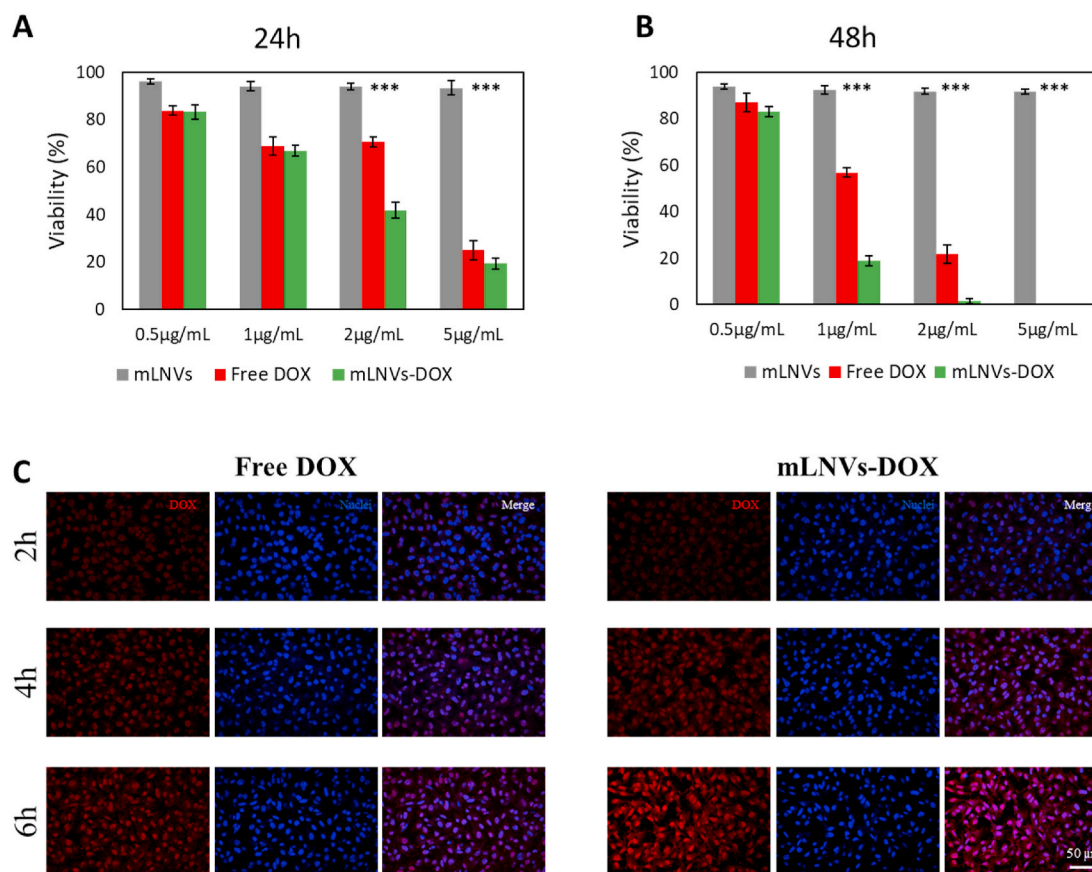
Fig. 3. *In vitro* studies. (A, B) Quantification of mLNVs cytotoxicity in melanoma cell cultures. Cells were exposed to a wide range (from 0.5 to 5 µg/mL) of DOX-equivalent mLNVs concentrations for 24 h and 48 h. Results are expressed as cell viability %. The data represent the mean value ± SD of triplicate cultures (*** = $t_{0.999}$). (C) Representative confocal microscopy images showing nuclear accumulation of DOX from free DOX and mLNVs-DOX exposure at a concentration of 2 µg/mL for 2, 4 and 6h. The columns show DOX fluorescence images (red), cell nuclei stained with Hoechst (blue) and the corresponding merged images. Magnification 10x. (For interpretation of the references to colour in this figure legend, the reader is referred to the Web version of this article.)

Table 2
IC_{50} values of mLNVs-DOX nanoparticles and free DOX in B16F10 melanoma cells.

Samples	24 h	48 h
Free DOX	3.9 µg/mL ± 0.9	1.5 µg/mL ± 0.6
mLNVs-DOX	1.7 µg/mL⁻ ± 0.6	0.9 µg/mL ± 0.2

the cytotoxicity when these cells were also exposed to magnetic hyperthermia (viability down to 40%). Under higher incubation concentration of mLNVs-DOX (1 µg DOX/mL, closer to optimal values), the results obtained showed that cytotoxicity reaches virtually 100% under a combination of mLNVs-DOX with hyperthermia (Figure S17). The number of living cells after the application of DOX plus MH was virtually cero which does not allow to quantify the full extent of the effect of this treatment combination. The effect of hyperthermia combined with mLNVs without DOX was also tested and the viability of melanoma cells dropped only to 80% after 1h AMF treatment. Close analysis of these viability data (Supporting Table 3) indicate that the combination of mLNVs-DOX and MH is more powerful than either of the two by themselves, showing a remarkable synergistic effect when encapsulation, chemotherapy (mLNVs-DOX) and thermotherapy (MH) are combined to treat melanoma cells.

Combining chemotherapy and hyperthermia enhances anti-tumor efficacy *in vivo*. Inspired by the satisfactory *in vitro* results, we explored the *in vivo* anticancer activity of each sample in a small animal *in vivo* model following the experimental design summarized in the

schematic illustration in Fig. 5A. In this context, we examined whether the combination of mLNVs-DOX and hyperthermia induced by AMF would be effective in a mouse model grafted with allotransplanted melanoma tumor onto the interscapular area. For the *in vivo* experiments, 7 days after malignant melanoma cell transplant, mice were randomly segregated into five groups to be treated with: saline (group 1), free DOX (group 2), mLNVs plus hyperthermia treatment (group 3), mLNVs-DOX (group 4) and mLNVs-DOX plus hyperthermia (group 5), in order to study the efficacy of mLNVs-DOX for enhanced chemo- and thermo-therapy. At 3 h post i. v. injection of each sample (dose of DOX = 2.5 mg/kg), mice in groups 3 and 5 were exposed to an alternating magnetic field (225 kHz, 20 mT) for 1 h. It is worth highlighting here that the selected dose of DOX (2.5 mg/kg) is between 2 and 6 times lower than the concentration frequently used in DOX studies (5–15 mg/kg). The rationale behind this 'low' dose considers the potential effect of the combination DOX-MH; an efficient delivery of DOX at high dose level could be sufficient to induce tumor regression and thus the extra effect sought through the application of MH would not be easily observable.

The anti-tumor effects of mLNVs were evaluated by monitoring the volume and weight of the melanoma tumor. Group 2 (free DOX) showed a similar effect on tumor growth to group 3 (thermotherapy alone). Treatment with mLNVs-DOX without hyperthermia (group 4, chemotherapy only) or exposed to hyperthermia (group 5, chemo-plus thermotherapy) displayed an obvious suppressive effect on tumor growth. In fact, group 5, mLNVs-DOX with hyperthermia, showed the slowest tumor growth and smallest volume (424 ± 38 mm^3) which was in average 3 and 2.1-fold smaller than the saline and free-DOX groups
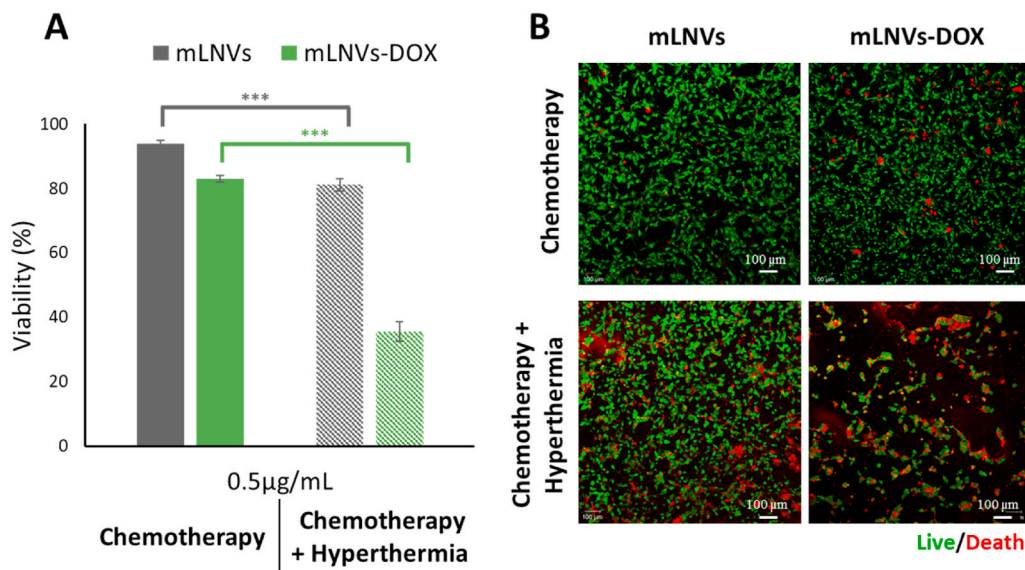
Fig. 4. Hyperthermia reduces malignant melanoma cell viability. (A) B16F10 melanoma cell viability after exposure to 0.5 µg/mL of mLNVs and mLNVs-DOX with (pattern fill) and without hyperthermia (solid fill). The data represent the mean value ± SD of triplicate cultures (*** = $t_{0.999}$). (B) Low resolution confocal microscopy projection images of calcein-AM and ethidium homodimer-I stained melanoma cells (green and red channels, respectively). Cells were treated with 0.5 µg/mL of mLNVs and mLNVs-DOX and with/ without hyperthermia. (For interpretation of the references to colour in this figure legend, the reader is referred to the Web version of this article.)
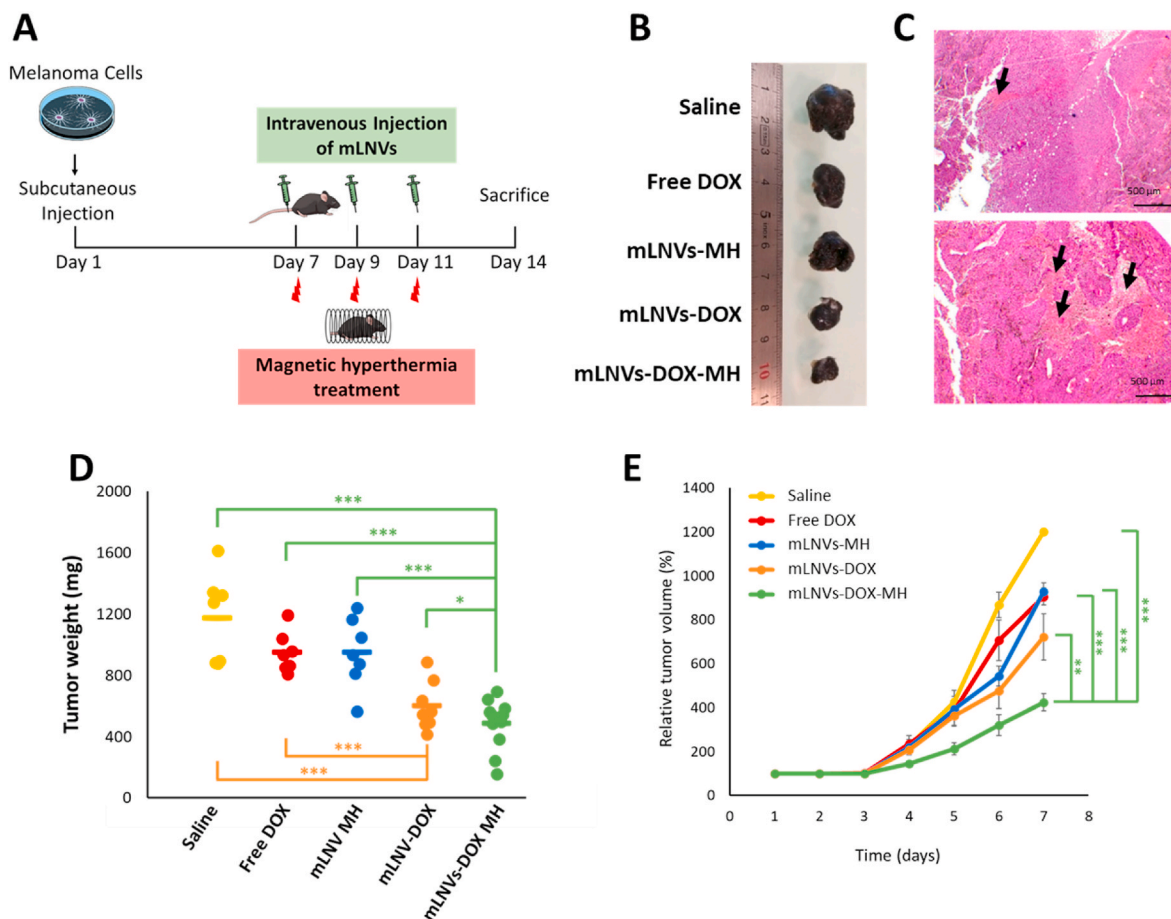
Fig. 5. *In vivo* efficacy of mLNVs. (A) Schematic illustration of the experimental design. (B) Representative images of tumors from the different treatment groups. (C) Hematoxylin-eosin stained tumor sections of mice treated with saline solution (top) and mLNVs-DOX (down). Images show details of the necrotic areas analyzed (arrows). (D) *Ex vivo* tumor weight of the different treatment groups at day 7, showing significantly smaller tumor sizes of the 'mLNVs DOX plus hyperthermia' group compared to the other groups (*** = $t_{0.999}$; * = $t_{0.9}$). (E) Changes in tumor volume with time for each group as the percentage of the initial tumor volume measured at the beginning of the treatment. Tumor volumes on day 1 were taken as 100%. The data represent the mean value ± SD of 8 animals per group (*** = $t_{0.999}$; ** = $t_{0.995}$).

(1200 ± 15 mm^3) (Fig. 5B, D and 5E). Notably, these statistically significant results indicate that mLNVs-DOX-MH possess the best antitumoral efficiency, thus reinforcing the synergistic effect results from the combined chemotherapy and thermotherapy observed *in vitro*.

Histopathological examination of the tumoral sections confirmed an important increase in the necrotic areas in tumors of mice treated with mLNVs-DOX with hyperthermia (5–7%) compared to the saline control group (1–2%) (Fig. 5C, S18) suggesting a nexus between tumor size and necrosis. It is worth mentioning here that this analysis is the common practice in the clinic for the follow-up of certain tumor types and in this case all samples were treated and analyzed by healthcare professionals in the exact same way real human samples are handled. Further analysis of liver, lung, and heart histological sections revealed the structural integrity of all tissues, thus indicating that our mLNVs did not exhibit any signs of toxicity in terms of tissue damage (Figure S19). Analysis of blood parameters in mice treated with saline, Free DOX and mLNVs-DOX-HT also show no significant changes (Figure S20).

It is noteworthy that besides the significant synergistic effect of the formulation, and in spite the lack of a specific targeting strategy, mLNVs-DOX nanocomposites accumulated in the tumoral organ as followed with several complementary techniques. On one hand we investigated the presence of the fluorescent dye (DiO) decorating the mLNVs. Fluorescent microscopy served to identify the particles in the processed tissues as small green spots close to the nuclei (Fig. 6A). On the other, we employed traditional Prussian Blue staining to identify ferric iron in tumor sections of mLNVs-DOX-MH treated mice (Fig. 6B). These two positives were corroborated quantitatively performing iron quantification analysis by ICP-OES in the tumors of treated mice (Fig. 6C). A biodistribution pattern was also obtained for the rest of the organs with

the expected results (Figure S21). The enhanced presence of Fe in the tumor was also used to follow the evolution of the tumors by MRI as described below.

mLNVs provide imaging capability by MRI. The presence of magnetic nanoparticles in the mLNVs formulation enables their use as contrast agents for T_2-weighted MR imaging. The same administration protocol designed for the treatment of melanoma was followed for the MRI studies. The tumor was located on the animals through fast spin echo T_2-weighted sequences, then divided into 4–6 slices (depending on the size) and a T_2 map was acquired (MEMS) for each tumor. ROIs of the tumor were manually delineated in each slice, the average and histogram of transversal relaxation times were obtained for each slice and combined (averaged) to get the final average T_2 of the tumor. As can be observed in Fig. 6E, the T_2 of tumors from animals treated with the mLNVs were in average over 15% shorter than those of control animal injected only with saline. This difference in contrast is remarkable considering that the total dose of Fe injected was around 800 μg Fe/kg, a similar dose to the one prescribed for Endorem (837 μg Fe/kg), and in this case the administration was divided into 3 injections over 6 days. The decrease in the relaxation time correlates well with the increase in Fe concentration observed in the tumors via ICP (44.1 *vs.* 60.1 mg Fe/g in saline *vs.* mLNVs-DOX groups) and in the Prussian blue staining of tumor sections (Fig. 6B). Representative T_2 maps of the tumors are shown in Fig. 6D, where differences in T_2 are depicted as darker pixels in the case of mLNVs-DOX administration. The histogram analysis of these tumors show a shift of the T_2 values to shorter times for mLNVs-DOX injected animals (Figure S22).
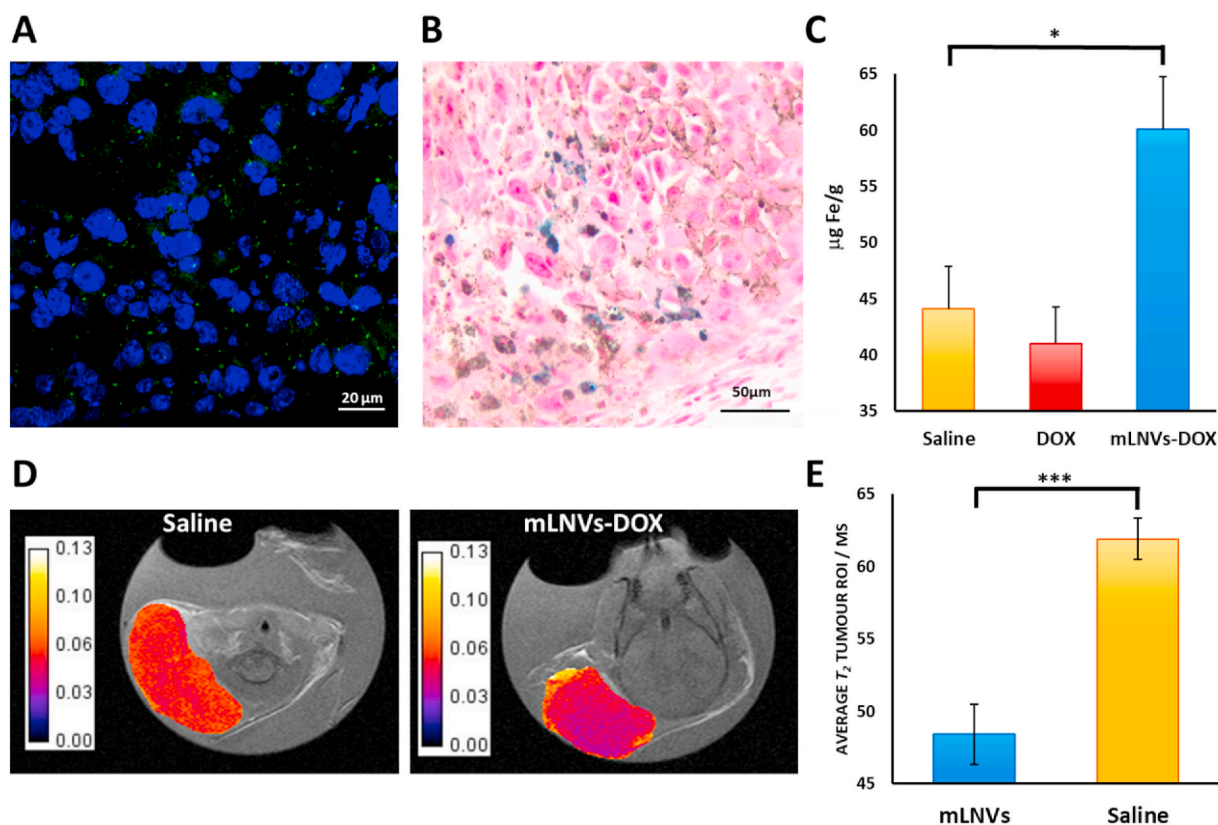

Fig. 6. (A) Representative fluorescence images of tumor slices collected from mLNVs-DOX treated mice. The nuclei were stained with Hoechst (blue) and mLNVs appear in green. (B) Representative Prussian blue staining of a tumor slice from a mice treated with mLNVs-DOX-MH. Blue spots indicate presence of iron in the tumor. (C) Fe quantification in the tumor by ICP-OES. The amount of Fe in the tumors of mLNVs-DOX treated mice is significantly higher than that in control animals (* = $t_{0.9}$). (D) Representative T_2 maps of tumors of saline (left) Vs. mLNVs-DOX (right) treated mice (scale bar represents T_2 in seconds). (E) Quantification of the average T_2 of the tumor of animals injected with saline (yellow) Vs. animals treated with mLNVs-DOX (blue) (*** = $t_{0.999}$). (For interpretation of the references to colour in this figure legend, the reader is referred to the Web version of this article.)

4. Conclusion

Here we developed an effective, green and simple method for the preparation of magnetic lipid nanocomposite vehicles from *Carnauba* wax with enhanced anticancer activity and low toxicity. This theranostic nanoplatform served to efficiently encapsulate magnetic nanoparticles and a chemotherapeutic drug, providing a longitudinal non-invasive imaging capability by MRI for the diagnosis and follow-up of the tumor, as well as a close control over the release profile of the drug through the combination of passive diffusion plus magnetic hyperthermia induction. Our results indicate that mLNVs show total biocompatibility whereas mLNVs-DOX display a remarkable dose-dependent cytotoxicity in malignant melanoma cells. *In vivo* animal studies also served to demonstrate that mLNVs-DOX display a significant anti-tumor activity. In addition, chemotherapy with mLNVs-DOX combined with AMF-induced hyperthermia, exhibited a strong cytotoxic effect in malignant melanoma cells both, *in vitro* and *in vivo*, even at relatively low DOX doses. The higher therapeutic activity provided by the developed mLNVs compared to the free drug relies in a series of interconnected events which, one after the other, converge in an improved therapeutic index. First, the solid hydrophobic wax matrix was able to accommodate a relatively high amount of DOX. Second, their suitable particle size and high colloidal stability in aqueous solution, together with their demonstrated biocompatibility, enable systemic administration and significant accumulation at the tumor site, presumably driven by the EPR effect. At the cellular level, tumor cells internalize the drug-loaded lipidic vehicles with high efficiency most likely through clathrin-mediated endocytosis, meaning that higher doses of drug (compared to free drug administration) reach the intracellular space and subsequently their therapeutic target, the nuclei. In addition to this efficient drug transport to the tumor cells and the derived improved cytotoxic effect, the magnetic component of the formulation (incorporated MNPs) plays a fundamental role enabling magnetic hyperthermia. The localized external stimulation of the mLNVs induce a local temperature increase in the surroundings of the encapsulated MNPs that triggers two essential mechanisms that feedback each other. On the one hand, the temperature increase modifies the drug delivery profile and accelerates the drug diffusion from the mLNVs. This induces an on-demand *in situ* drug burst that precipitates drug accumulation in cancer cells, enhancing therapeutic activity and also helping avoid potential drug resistance phenomena. On the other hand, this local heat generation not only activates apoptotic/necrotic cell death pathways *per se*, but also sensitize tumor cells to cancer chemotherapy. Altogether, these mechanisms account for the synergistic thermochemo-therapeutic activity observed both *in vitro* and *in vivo*. Therefore, here we demonstrate that the combination of chemotherapy with thermotherapy can establish a synergistic platform for treatment of solid tumors under lower drug dosing schemes through a drug delivery system systemically administered, which may realize the dual goals of reduced systemic toxicity and enhanced anti-tumoral efficacy. In addition, we find it relevant to highlight here that during the reviewing process of the manuscript, another study by our group was published that evidences that the sustained release of the drug upon particle arrival to the target tissue, results in a significant anti-metastatic effect [66]. This sustained *in situ* release effect allows an improved local efficacy and reduced toxicity, compared to that reported for liposomal formulations where the release is faster, causing possible adverse effects such as palmoplantar erythrodysesthesia syndrome.

CRediT authorship contribution statement

Lorena García-Hevia: Methodology, Investigation, Validation, Resources, Formal analysis, Visualization, Writing – original draft. **Íñigo Casafont:** Investigation, Resources, Writing – review & editing. **Jessica Oliveira:** Investigation. **Nuria Terán:** Investigation. **Mónica L. Fanarraga:** Resources, Supervision, Writing – review & editing. **Juan Gallo:** Conceptualization, Methodology, Investigation, Validation, Resources, Supervision, Writing – original draft. **Manuel Bañobre-López:** Conceptualization, Methodology, Resources, Visualization, Supervision, Writing – review & editing, Project administration, Funding acquisition.

Declaration of competing interest

The authors declare no conflict of interest.

Acknowledgments

Appendix A. Supplementary data

Supplementary data to this article can be found online at https://doi.org/10.1016/j.bioactmat.2021.06.009.

References

[1] S. Senapati, A.K. Mahanta, S. Kumar, P. Maiti, Controlled drug delivery vehicles for cancer treatment and their performance, Signal Transduct. Target. Ther. 3 (2018), 7.

[2] G. Housman, S. Byler, S. Heerboth, K. Lapinska, M. Longacre, N. Snyder, S. Sarkar, Drug resistance in cancer: an overview, Cancers 6 (2014) 1769–1792.

[3] J.M. Brown, Tumor hypoxia in cancer therapy, in: Methods Enzymol., 2007, pp. 295–321.

[4] K. Park, Facing the truth about nanotechnology in drug delivery, ACS Nano 7 (2013) 7442–7447.

[5] J.I. Hare, T. Lammers, M.B. Ashford, S. Puri, G. Storm, S.T. Barry, Challenges and strategies in anti-cancer nanomedicine development: an industry perspective, Adv. Drug Deliv. Rev. 108 (2017) 25–38.

[6] Y. Barenholz, Doxil® - the First FDA-Approved Nano-Drug: Lessons Learned, J. Control. Release, 2012.

[7] Compositions and Methods of Delivery of Pharmacological Agents, 2003.

[8] Y.(Chezy, Barenholz, Doxil® — the first FDA-approved nano-drug: lessons learned, J. Contr. Release 160 (2012) 117–134.

[9] N. Koleini, B.E. Nickel, A.L. Edel, R.R. Fandrich, A. Ravandi, E. Kardami, Oxidized phospholipids in Doxorubicin-induced cardiotoxicity, Chem. Biol. Interact. 303 (2019) 35–39.

[10] P.B. Chapman, A. Hauschild, C. Robert, J.B. Haanen, P. Ascierto, J. Larkin, R. Dummer, C. Garbe, A. Testori, M. Maio, D. Hogg, P. Lorigan, C. Lebbe, T. Jouary, D. Schadendorf, A. Ribas, S.J. O'Day, J.A. Sosman, J.M. Kirkwood, A.M. M. Eggermont, B. Dreno, K. Nolop, J. Li, B. Nelson, J. Hou, R.J. Lee, K.T. Flaherty, G.A. McArthur, Improved survival with vemurafenib in melanoma with BRAF V600E mutation, N. Engl. J. Med. 364 (2011) 2507–2516.

[11] F.S. Hodi, S.J. O'Day, D.F. McDermott, R.W. Weber, J.A. Sosman, J.B. Haanen, R. Gonzalez, C. Robert, D. Schadendorf, J.C. Hassel, W. Akerley, A.J.M. van den Eertwegh, J. Lutzky, P. Lorigan, J.M. Vaubel, G.P. Linette, D. Hogg, C. H. Ottensmeier, C. Lebbé, C. Peschel, I. Quirt, J.I. Clark, J.D. Wolchok, J.S. Weber, J. Tian, M.J. Yellin, G.M. Nichol, A. Hoos, W.J. Urba, Improved survival with ipilimumab in patients with metastatic melanoma, N. Engl. J. Med. 363 (2010) 711–723.

[12] C. Robert, L. Thomas, I. Bondarenko, S. O'Day, J. Weber, C. Garbe, C. Lebbe, J.-F. Baurain, A. Testori, J.-J. Grob, N. Davidson, J. Richards, M. Maio, A. Hauschild, W.H. Miller, P. Gascon, M. Lotem, K. Harmankaya, R. Ibrahim, S. Francis, T.-

T. Chen, R. Humphrey, A. Hoos, J.D. Wolchok, Ipilimumab plus dacarbazine for previously untreated metastatic melanoma, N. Engl. J. Med. 364 (2011) 2517–2526.

[13] F.K.H. van Landeghem, K. Maier-Hauff, A. Jordan, K.T. Hoffmann, U. Gneveckow, R. Scholz, B. Thiesen, W. Brück, A. von Deimling, Post-mortem studies in glioblastoma patients treated with thermotherapy using magnetic nanoparticles, Biomaterials 30 (2009) 52–57.

[14] K. Maier-Hauff, F. Ulrich, D. Nestler, H. Niehoff, P. Wust, B. Thiesen, H. Orawa, V. Budach, A. Jordan, Efficacy and safety of intratumoral thermotherapy using magnetic iron-oxide nanoparticles combined with external beam radiotherapy on patients with recurrent glioblastoma multiforme, J. Neuro Oncol. 103 (2011) 317–324.

[15] Y. Qu, J. Li, J. Ren, J. Leng, C. Lin, D. Shi, Enhanced synergism of thermo-chemotherapy by combining highly efficient magnetic hyperthermia with magnetothermally-facilitated drug release, Nanoscale 6 (2014) 12408–12413.

[16] E. Millart, S. Lesieur, V. Faivre, Superparamagnetic lipid-based hybrid nanosystems for drug delivery, Expet Opin. Drug Deliv. 15 (2018) 523–540.

[17] H.C. Kim, E. Kim, S.W. Jeong, T.L. Ha, S.I. Park, S.G. Lee, S.J. Lee, S.W. Lee, Magnetic nanoparticle-conjugated polymeric micelles for combined hyperthermia and chemotherapy, Nanoscale 7 (2015) 16470–16480.

[18] S. Kossatz, J. Grandke, P. Couleaud, A. Latorre, A. Aires, K. Crosbie-Staunton, R. Ludwig, H. Dähring, V. Ettelt, A. Lazaro-Carrillo, M. Calero, M. Sader, J. Courty, Y. Volkov, A. Prina-Mello, A. Villanueva, Á. Somoza, A.L. Cortajarena, R. Miranda, I. Hilger, Efficient treatment of breast cancer xenografts with multifunctionalized iron oxide nanoparticles combining magnetic hyperthermia and anti-cancer drug delivery, Breast Cancer Res. 17 (2015), 66.

[19] M. Gogoi, M. Jaiswal, H. Sarma, D.B. Bahadur, R. Banerjee, Biocompatibility and therapeutic evaluation of magnetic liposomes designed for self-controlled cancer hyperthermia and chemotherapy, Academic.Oup.Com 9 (6) (2017) 555–565.

[20] T.T.H. Le, T.Q. Bui, T.M.T. Ha, M.H. Le, H.N. Pham, P.T. Ha, Optimizing the alginate coating layer of doxorubicin-loaded iron oxide nanoparticles for cancer hyperthermia and chemotherapy, J. Mater. Sci. 53 (2018) 13826–13842.

[21] C. Tapeinos, A. Marino, M. Battaglini, S. Migliorin, R. Brescia, A. Scarpellini, C. De Julián Fernández, M. Prato, F. Drago, G. Ciofani, Stimuli-responsive lipid-based magnetic nanovectors increase apoptosis in glioblastoma cells through synergic intracellular hyperthermia and chemotherapy, Nanoscale 11 (2019) 72–88.

[22] D.C. Phung, H.T. Nguyen, T.T. Phuong Tran, S.G. Jin, C.S. Yong, D.H. Truong, T. H. Tran, J.O. Kim, Combined hyperthermia and chemotherapy as a synergistic anticancer treatment, J. Pharm. Investig. 49 (2019) 519–526.

[23] Y. Jin, X. Liang, Y. An, Z. Dai, Microwave-triggered smart drug release from liposomes Co-encapsulating doxorubicin and salt for local combined hyperthermia and chemotherapy of cancer, Bioconjugate Chem. 27 (2016) 2931–2942.

[24] P. Pradhan, J. Giri, F. Rieken, C. Koch, O. Mykhaylyk, M. Döblinger, R. Banerjee, D. Bahadur, C. Plank, Targeted temperature sensitive magnetic liposomes for thermo-chemotherapy, J. Contr. Release 142 (2010) 108–121.

[25] R.O. Rodrigues, G. Baldi, S. Doumett, L. Garcia-Hevia, J. Gallo, M. Bañobre-López, G. Dražić, R.C. Calhelha, I.C.F.R. Ferreira, R. Lima, H.T. Gomes, A.M.T. Silva, Multifunctional graphene-based magnetic nanocarriers for combined hyperthermia and dual stimuli-responsive drug delivery, Mater. Sci. Eng. C 93 (2018) 206–217.

[26] E. Christodoulou, M. Nerantzaki, S. Nanaki, P. Barmpalexis, K. Giannousi, C. Dendrinou-Samara, M. Angelakeris, E. Gounari, A.D. Anastasiou, D.N. Bikiaris, Paclitaxel magnetic core–shell nanoparticles based on poly(Lactic acid) semitelechelic novel block copolymers for combined hyperthermia and chemotherapy treatment of cancer, Pharmaceutics 11 (2019), 213.

[27] R.V. Ferreira, T.M.D.M. Martins, A.M. Goes, J.D. Fabris, L.C.D. Cavalcante, L.E. F. Outon, R.Z. Domingues, Thermosensitive gemcitabine-magnetoliposomes for combined magnetic hyperthermia and chemotherapy, Nanotechnology 27 (2016).

[28] B. Clares, R.A. Biedma-Ortiz, E. Sáez-Fernández, J.C. Prados, C. Melguizo, L. Cabeza, R. Ortiz, J.L. Arias, Nano-engineering of 5-fluorouracil-loaded magnetoliposomes for combined hyperthermia and chemotherapy against colon cancer, Eur. J. Pharm. Biopharm. 85 (2013) 329–338.

[29] S.E. Minaei, S. Khoei, S. Khoee, F. Vafashoar, V.P. Mahabadi, In vitro anti-cancer efficacy of multi-functionalized magnetite nanoparticles combining alternating magnetic hyperthermia in glioblastoma cancer cells, Mater, Sci. Eng. C. 101 (2019) 575–587.

[30] B.T. Mai, P.B. Balakrishnan, M.J. Barthel, F. Piccardi, D. Niculaes, F. Marinaro, S. Fernandes, A. Curcio, H. Kakwere, G. Autret, R. Cingolani, F. Gazeau, T. Pellegrino, Thermoresponsive iron oxide nanocubes for an effective clinical translation of magnetic hyperthermia and heat-mediated chemotherapy, ACS Appl. Mater. Interfaces 11 (2019) 5727–5739.

[31] Y.S. Ong, M. Bañobre-López, S.A. Costa Lima, S. Reis, A multifunctional nanomedicine platform for co-delivery of methotrexate and mild hyperthermia towards breast cancer therapy, Mater. Sci. Eng. C 116 (2020), 111255.

[32] D. Liu, Y. Hong, Y. Li, C. Hu, T.C. Yip, W.K. Yu, Y. Zhu, C.C. Fong, W. Wang, S. K. Au, S. Wang, M. Yang, Targeted destruction of cancer stem cells using multifunctional magnetic nanoparticles that enable combined hyperthermia and chemotherapy, Theranostics 10 (2020) 1181–1196.

[33] I. Sato, M. Umemura, K. Mitsudo, H. Fukumura, J.K.-S. reports, undefined, Simultaneous hyperthermia-chemotherapy with controlled drug delivery using single-drug nanoparticles, Nat. Can. (2016).

[34] A. Singh, S. Jain, S.S.-M.S., E. C, U, Magnetic Nanoparticles for Amalgamation of Magnetic Hyperthermia and Chemotherapy: an Approach towards Enhanced Attenuation of Tumor, vol. 110, Elsevier, 2020.

[35] A. Papadaki, A. Mallouchos, M.-N. Efthymiou, C. Gardeli, N. Kopsahelis, E.C. G. Aguieiras, D.M.G. Freire, S. Papanikolaou, A.A. Koutinas, Production of wax

[36] esters via microbial oil synthesis from food industry waste and by-product streams, Bioresour. Technol. 245 (2017) 274–282.

M.M. Fiume, B.A. Heldreth, W.F. Bergfeld, D.V. Belsito, R.A. Hill, C.D. Klaassen, D. C. Liebler, J.G. Marks, R.C. Shank, T.J. Slaga, P.W. Snyder, F.A. Andersen, Safety assessment of alkyl esters as used in cosmetics, Int. J. Toxicol. 34 (2015) 5S–69S.

[37] J. Milanovic, V. Manojlovic, S. Levic, N. Rajic, V. Nedovic, B. Bugarski, Microencapsulation of flavors in carnauba wax, Sensors 10 (2010) 901–912.

[38] A.R. Madureira, D.A. Campos, P. Fonte, S. Nunes, F. Reis, A.M. Gomes, B. Sarmento, M.M. Pintado, Characterization of solid lipid nanoparticles produced with carnauba wax for rosmarinic acid oral delivery, RSC Adv. 5 (2015) 22665–22673.

[39] I.-H. Kim, H. Lee, J.E. Kim, K. Bin Song, Y.S. Lee, D.S. Chung, S.C. Min, Plum coatings of lemongrass oil-incorporating carnauba wax-based nanoemulsion, J. Food Sci. 78 (2013) E1551–E1559.

[40] J.R. Bertino, Encyclopedia of Cancer, Academic Press, 2002.

[41] Estimated Numbers of New Cancer Cases for 2017, Excluding Basal Cell and Squamous Cell Skin Cancers and in Situ carcinomas except urinary bladder.

[42] M.B. Lens, M. Dawes, Global perspectives of contemporary epidemiological trends of cutaneous malignant melanoma, Br. J. Dermatol. 150 (2004) 179–185.

[43] F.B. Bombelli, C.A. Webster, M. Moncrieff, V. Sherwood, The scope of nanoparticle therapies for future metastatic melanoma treatment, Lancet Oncol. 15 (2014) e22–e32.

[44] C. Sun, L. Wang, S. Huang, G.J.J.E. Heynen, A. Prahallad, C. Robert, J. Haanen, C. Blank, J. Wesseling, S.M. Willems, D. Zecchin, S. Hobor, P.K. Bajpe, C. Lieftink, C. Mateus, S. Vagner, W. Grernrum, I. Hofland, A. Schlicker, L.F.A. Wessels, R. L. Beijersbergen, A. Bardelli, F. Di Nicolantonio, A.M.M. Eggermont, R. Bernards, Reversible and adaptive resistance to BRAF(V600E) inhibition in melanoma, Nature 508 (2014) 118–122.

[45] K. Trunzer, A.C. Pavlick, L. Schuchter, R. Gonzalez, G.A. McArthur, T.E. Hutson, S. J. Moschos, K.T. Flaherty, K.B. Kim, J.S. Weber, P. Hersey, G.V. Long, D. Lawrence, P.A. Ott, R.K. Amaravadi, K.D. Lewis, I. Puzanov, R.S. Lo, A. Koehler, M. Kockx, O. Spleiss, A. Schell-Steven, H.N. Gilbert, L. Cockey, G. Bollag, R.J. Lee, A.K. Joe, J. A. Sosman, A. Ribas, Pharmacodynamic effects and mechanisms of resistance to vemurafenib in patients with metastatic melanoma, J. Clin. Oncol. 31 (2013) 1767–1774.

[46] M. Das Thakur, F. Salangsang, A.S. Landman, W.R. Sellers, N.K. Pryer, M. P. Levesque, R. Dummer, M. McMahon, D.D. Stuart, Modelling vemurafenib resistance in melanoma reveals a strategy to forestall drug resistance, Nature 494 (2013) 251–255.

[47] P. Silva, B. Bonifácio, M. Ramos, K. Negri, T. Maria Bauab, M. Chorilli, Nanotechnology-based drug delivery systems and herbal medicines: a review, Int. J. Nanomed. 9 (2013), 1.

[48] R.M. Mainardes, M.C.C. Urban, P.O. Cinto, M.V. Chaud, R.C. Evangelista, M.P. D. Gremião, Liposomes and micro/nanoparticles as colloidal carriers for nasal drug delivery, Curr. Drug Deliv. 3 (2006) 275–285.

[49] R.N. Saha, V. Vasanthakumar, G. Bende, M. Snehalatha, Nanoparticulate drug delivery systems for cancer chemotherapy, Mol. Membr. Biol. 27 (2010) 215–231.

[50] J. Venugopal, M.P. Prabhakaran, S. Low, A.T. Choon, G. Deepika, V.R.G. Dev, S. Ramakrishna, Continuous nanostructures for the controlled release of drugs, Curr. Pharmaceut. Des. 15 (2009) 1799–1808.

[51] A.E. Grill, N.W. Johnston, T. Sadhukha, J. Panyam, A review of select recent patents on novel nanocarriers, Recent Pat. Drug Deliv. Formulation 3 (2009) 137–142.

[52] C.L. Moura, J. Gallo, L. García-Hevia, O.D.L. Pessoa, N.M.P.S. Ricardo, M. Bañobre-López, Magnetic hybrid wax nanocomposites as externally controlled theranostic vehicles: high MRI enhancement and synergistic magnetically assisted thermo/chemo therapy, Chem. Eur. J. 26 (2020) 4531–4538.

[53] R.R. De Almeida, J. Gallo, A.C.C. Da Silva, A.K.O. Da Silva, O.D.L. Pessoa, T. G. Araújo, L.K.A.M. Leal, P.B.A. Fechine, M. Bañobre-López, N.M.P.S. Ricardo, Preliminary evaluation of novel triglyceride-based nanocomposites for biomedical applications, J. Braz. Chem. Soc. 28 (2017) 1–10.

[54] L. García-Hevia, F. Fernández, I. Casafont, J.C. Villegas, M.L. Fanarraga, A fast, reliable and cost-effective method to generate tumor organs for therapy screening in vivo, Biomed, Phys. Eng. Express. 2 (2016), 035009.

[55] K.K. Karukstis, E.H. Thompson, J.A. Whiles, R.J. Rosenfeld, Deciphering the fluorescence signature of daunomycin and doxorubicin, Biophys. Chem. 73 (1998) 249–263.

[56] M. Rohrer, H. Bauer, J. Mintorovitch, M. Requardt, H.-J. Weinmann, Comparison of magnetic properties of MRI contrast media solutions at different magnetic field strengths, Invest. Radiol. 40 (2005).

[57] G. Kandasamy, A. Sudame, P. Bhati, A. Chakrabarty, D. Maity, Systematic investigations on heating effects of carboxyl-amine functionalized superparamagnetic iron oxide nanoparticles (SPIONs) based ferrofluids for in vitro cancer hyperthermia therapy, J. Mol. Liq. 256 (2018) 224–237.

[58] A. Hervault, A.E. Dunn, M. Lim, C. Boyer, D. Mott, S. Maenosono, N.T.K. Thanh, Doxorubicin loaded dual pH- and thermo-responsive magnetic nanocarrier for combined magnetic hyperthermia and targeted controlled drug delivery applications, Nanoscale 8 (2016) 12152–12161.

[59] X.L. Liu, Y. Yang, C.T. Ng, L.Y. Zhao, Y. Zhang, B.H. Bay, H.M. Fan, J. Ding, Magnetic vortex nanorings: a new class of hyperthermia agent for highly efficient in vivo regression of tumors, Adv. Mater. 27 (2015) 1939–1944.

[60] J. Mohapatra, M. Xing, J.P. Liu, Inductive thermal effect of ferrite magnetic nanoparticles, Materials 12 (2019), 3208.

[61] C. Blanco-Andujar, D. Ortega, P. Southern, Q.A. Pankhurst, N.T.K. Thanh, High performance multi-core iron oxide nanoparticles for magnetic hyperthermia:

microwave synthesis, and the role of core-to-core interactions, Nanoscale 7 (2015) 1768–1775.

[62] I. Andreu, E. Natividad, L. Solozábal, O. Roubeau, Nano-objects for addressing the control of nanoparticle arrangement and performance in magnetic hyperthermia, ACS Nano 9 (2015) 1408–1419.

[63] T.E. Torres, E. Lima, M.P. Calatayud, B. Sanz, A. Ibarra, R. Fernández-Pacheco, A. Mayoral, C. Marquina, M.R. Ibarra, G.F. Goya, The relevance of Brownian relaxation as power absorption mechanism in Magnetic Hyperthermia, Sci. Rep. 9 (2019), 3992.

[64] R. Grillo, J. Gallo, D.G. Stroppa, E. Carbó-Argibay, R. Lima, L.F. Fraceto, M. Bañobre-López, Sub-micrometer magnetic nanocomposites: insights into the effect of magnetic nanoparticles interactions on the optimization of SAR and MRI performance, ACS Appl. Mater. Interfaces 8 (2016) 25777–25787.

[65] R. Matteoni, T.E. Kreis, Translocation and clustering of endosomes and lysosomes depends on microtubules, J. Cell Biol. 105 (1987) 1253–1265.

[66] L. Valdivia, L. García-Hevia, M. Bañobre-López, J. Gallo, R. Valiente, M. L. Fanarraga, Solid-lipid particles for lung metastasis treatment, Pharmaceutics 13 (2021), 93.